Role of Defects in the Photoluminescence and Photoresponse of WS_2–Graphene Heterodevices

Min-Wen Yu[1,6,#], Yu-Tang Lin[2,#], Chia-Hung Wu[1], Tung-Jung Wang[3], Jhuang-Hao Cyue[4], Jun Kikkawa[5], Satoshi Ishii[6], Tien-Chang Lu[7], and Kuo-Ping Chen[8,9]*

[1]College of Photonics, National Yang Ming Chiao Tung University, 301 Gaofa 3rd Road, Tainan 71150, Taiwan

[2]Graduate Degree Program of Photonic Technology, National Yang Ming Chiao Tung University, 301 Gaofa 3rd Road, Tainan 71150, Taiwan

[3]Institute of Lighting and Energy Photonics, College of Photonics, National Yang Ming Chiao Tung University, 301 Gaofa 3rd Road, Tainan 71150, Taiwan

[4]Institute of Photonic System, College of Photonics, National Yang Ming Chiao Tung University, 301 Gaofa 3rd Road, Tainan 71150, Taiwan

[5]Research Center for Advanced Measurement and Characterization, National Institute for Materials Science, 1-1 Namiki, Tsukuba 305-0044, Japan

[6]International Center for Materials Nanoarchitectonics (MANA), National Institute for Materials Science (NIMS), 1-1 Namiki, Tsukuba, Ibaraki 305-0044, Japan

[7]Department of Photonics, College of Electrical and Computer Engineering, National Yang Ming Chiao Tung University, Hsinchu 30010, Taiwan

[8] Institute of Photonics Technologies, National Tsing Hua University, Hsinchu 30013, Taiwan Institute of

[9] Imaging and Biomedical Photonic, College of Photonics, National Yang Ming Chiao Tung University, 301 Gaofa 3rd Road, Tainan 71150, Taiwan

[#] Equally contributed

* Email address: kpchen@ee.nthu.edu.tw

KEYWORDS: tungsten disulfide (WS_2), graphene, photodetector, sulfur vacancy, photoluminescence

ABSTRACT

Two-dimensional (2D) transition metal dichalcogenides are promising materials for next-generation photodetectors. Therefore, controlling point chalcogen vacancies in chemical vapor deposition (CVD) synthesis is inevitable. In this work, the number of sulfur vacancies in monolayer WS_2 flakes is well controlled in CVD synthesis, which resulted in a photoluminescence (PL) intensity difference. In addition, the relationship between the PL intensity and photoresponse of monolayer WS_2 on graphene is discussed. The sulfur vacancies introduce defect trap states that cause carrier recombination and reduce carrier drift to graphene, thus decreasing the photocurrent. Furthermore, the gate-tunable Fermi level of graphene allows tunable responsivity of the WS_2–graphene photodetector of up to 5 A/W with metal hard-mask fabrication. Our findings on the PL intensity and responsivity provide a simple and efficient strategy for choosing high-performance CVD-synthesized 2D TMD photodetectors.

1. Introduction

With the rapid growth of traditional three-dimensional (3D) silicon semiconductor manufacturing, the limitation of physical and semiconductor processes at the 2-nm technology node is quickly approaching. Atomically thin two-dimensional (2D) materials exhibit superior electrical and optical properties that can support the 3D silicon semiconductor process when the device is scaled down to the technology node of 1 nm.[1, 2] Consequently, for the next generation of ultrathin optoelectronic devices, 2D semiconductor-based photodetectors have attracted considerable interest. In addition, a single layer of a 2D material consists of a covalently bonded lattice with extraordinary electronic and optical properties, in contrast to 3D semiconductors that have dangling bonds and trap states at the surface, which decrease carrier mobility. In general, 2D materials interact between neighboring layers via van der Waals (vdW) forces, which allow

vertical stacking onto vdW materials to form heterostructures without the constraints of crystal lattice matching. Furthermore, these vdW materials can be integrated with silicon photonic platforms such as light emitters, modulators, and photodetectors.

Among the family of 2D photodetectors, graphene phototransistors have been widely studied and reported[3, 4] owing to their fascinating optoelectronic properties such as fast response time, high carrier mobility, and ultra-broadband absorption. However, the zero bandgap and ultrathin thickness (~0.3 nm) make graphene a weak light absorber with low responsivity. A different class of 2D materials that can overcome this limitation are transition-metal dichalcogenides (TMDs). These materials have the general formula MX_2, where M is a transition metal (such as Mo, W, Re) and X is a chalcogen (such as S, Se, Te). Unlike semimetallic graphene, TMDs monolayers such as MoS_2 and WS_2 are direct bandgap semiconductors. This property gives them remarkable electronic and optoelectronic advantages[5] over graphene . Besides, TMDs also offer several benefits for optoelectronic devices, such as photodetectors[6-9], light-emitting diodes (LEDs)[10-12], lasers[13], modulators[14], and solar cells[15, 16]. These devices can exploit the unique properties of TMDs to achieve high performance and novel functionalities.

However, WS_2 and MoS_2 photodetectors have relatively slow response times. In addition, a Schottky barrier is usually formed depending on the electrode material. Recently, it has been reported that an ohmic contact is formed between semimetal bismuth and TMDs; this significantly reduces contact resistance.[17] The above results demonstrate that both graphene and TMDs have their specific advantages for photodetector applications.

In this study, we fabricated a monolayer WS_2-on-graphene (WS_2/G) heterostructure photodetector,[18-20] where monolayer graphene is a photoconductor and carries photoexcited carriers from monolayer WS_2. In addition, the contact resistance between the metal electrode and

graphene was found to be less than that of the Schottky junction of metal/WS_2, which allowed more carriers to be driven in this device.

To improve the optoelectronic property of WS2/graphene photodetector, strain effects have been widely applied to overcome the limitations of detection range. Strain can alter the bandgap of WS_2 by deforming its crystal lattice, and thus extend its absorption wavelength limit for broadband application.[21, 22] Strain can also increase the mobility of charge carriers (electrons and holes) by applying appropriate strain[23], which can improve the device response time performance. Doping effects are also an important factor that can influence the optoelectronic properties of WS_2/G photodetector, besides strain effects. The band gap, the carrier concentration, the charge transfer, and the defect density of WS_2 can be modulated by doping, according to some studies[24-26]. Hence, strain and doping effects are both crucial for tuning the optoelectronic properties of WS_2/G photodetectors and optimizing their performance.

Although the mechanical exfoliation of bulk WS_2 can be used to prepare high-quality monolayer WS_2, scalability and thickness management limit practical applications. However, the small device area and fabrication uncertainty limit the progress of industrial applications. To date, various approaches have been studied for the synthesis of TMD materials; these include atomic layer deposition[27, 28] metal–organic chemical vapor deposition[29, 30] and chemical vapor deposition (CVD).[31-34] Owing to its low cost and highly controllable properties, powder CVD has become a preferred approach for synthesizing TMD materials. In this process, both powder precursors of transition-metal oxides (e.g., MoO_3 and WO_3) and chalcogen elements (e.g., sulfur, selenium, and tellurium) are introduced in the heating furnace for TMD material growth, and Ar or N_2 gas is utilized as a carrier gas to transport sulfur steam for sulfurization. Another sulfurization precursor,

H_2S, is expected to improve surface uniformity. Despite remarkable progress in TMD synthesis, the formation of defects during growth has rarely been investigated. In particular, the largest group of defects in WS_2 is sulfur vacancies, which induce carrier scattering and doping effects. These sulfur vacancies play an important role in determining the photoluminescence (PL) quantum yield and electrical properties.

In this work, we measured the PL intensity of various monolayer WS_2 flakes on graphene to form a WS_2–graphene photodetector and elucidate the relationship between the PL intensity and photocurrent. The controllable PL intensity of the monolayer WS_2 flakes was achieved by changing the H_2S flow rate. The photoexcited electron–hole pairs were separated at the WS_2 and graphene interfaces, where the carriers are driven and collected by the built-in electric fields. Then, external electric fields were applied to the devices to investigate the photocurrent on various PL intensities of the monolayer WS_2 flakes. In addition, a photodetector based on the WS_2–graphene heterostructure can achieve photoresponsivity tunability from zero to 5 A/W with a low-cost metal hard mask.

2. Methodology

Growth and transfer of monolayer WS_2 flakes. A 4-inch SiO_2/Si (300-nm SiO_2) substrate was treated with UV light and ozone for 30 min to obtain a highly hydrophilic surface. Then, ~5 ml of a 25 mM Na_2WO_4 aqueous solution was spin-coated on the substrate at 3000 rpm for 60 s. Subsequently, the substrate was loaded into the center of the CVD heating zone. After sealing, the furnace was heated to 840 ℃ in 30 min with 200 sccm of high-purity Ar and 10 sccm H_2 (step I in Figure S2). During the annealing step (step II in Figure S2), the temperature was maintained at 840 ℃ for 30 min. Finally, during the sulfurization step (step III in Figure S2), 200 sccm of Ar,

10 sccm of H_2, and 5 sccm of H_2S were introduced into the furnace, and the reaction was completed in 2 min. In addition, three different H_2S flow rates (5, 10, and 15 sccm) were tested (Figure S4).

To transfer the as-grown monolayer WS_2 flakes onto the target substrates, the as-grown monolayer WS_2 was coated with a layer of PMMA. The PMMA/WS_2 films were then peeled off from the growth substrate using a 0.5 M NaOH solution as the etchant. The PMMA/WS_2 film was diluted with deionized water and used as the target substrate. Finally, PMMA was removed by sequentially rinsing the target substrate with acetone and isopropanol.

Device fabrication and optoelectronic measurement. Monolayer graphene was transferred onto an SiO_2/Si substrate (with a SiO_2 thickness of 300 nm) using the wet transfer method. The monolayer WS_2 flakes with different PL intensities were then transferred onto a graphene/SiO_2/Si substrate. The Au electrodes were defined using a shadow mask and deposited using electron gun deposition. Electrical measurements were conducted in a probe station equipped with a Keysight B2901A source meter. A 532-nm CW laser was used as the light source for the photocurrent measurement.

Raman and PL characterization. Raman and PL signals were acquired using a confocal Raman system (Jobin Yvon/Labram HR) and excited using a 532-nm CW laser operated at 0.8 mW. The signals were collected using a 50× objective lens (Olympus, MPLN) with a numerical aperture of 0.75 and the excitation signal was blocked using 532-notch filter, which was resolved using an 1800 g/mm grating and recorded using a spectrometer. All the measurements were performed at room temperature.

Scanning electron microscopy (SEM) characterization. The SEM images were obtained using a focused-ion-beam (FEI Helios NanoLabG3 CX, NCKU, Taiwan) instrument in SEM mode with

an acceleration voltage of 2 kV and a current of 98 pA. The optical and electrical characterization was performed before taking the SEM images to avoid electron doping or sample damage.

STEM characterization. Monolayer WS_2 flakes were transferred onto holey carbon films (R2/2 Mo; QUANTIFOIL). HAADF–STEM observations were performed using an electron microscope (Thermo Fisher Scientific, Inc.) at room temperature. The beam energy, probe current, convergence semi-angle, and collection range were 80 keV, 20 pA, 25 mrad, and 69–200 mrad, respectively. A high-pass filter was applied to the raw images, followed by Gaussian blurring, to obtain the final images.

3. Results and discussion

Defects in TMD materials, including vacancies, impurities, and adatoms, can be naturally or artificially generated.[35] Sulfur vacancies comprise the largest defect group in WS_2, and they are naturally formed in the CVD process. Figure 1 shows a schematic of the WS_2 sulfur vacancy configuration. The sulfur vacancy introduces an unoccupied defect state (V_{S1}) and an occupied defect state (V_{S2}) located close to the valance gap and in the bandgap,[36, 37] where a fraction of photoexcited electrons (or holes) can be trapped by the electron trap states (or hole trap states). These defect-bound excitons, if radiatively recombined, lead to an increase in overall PL intensity.

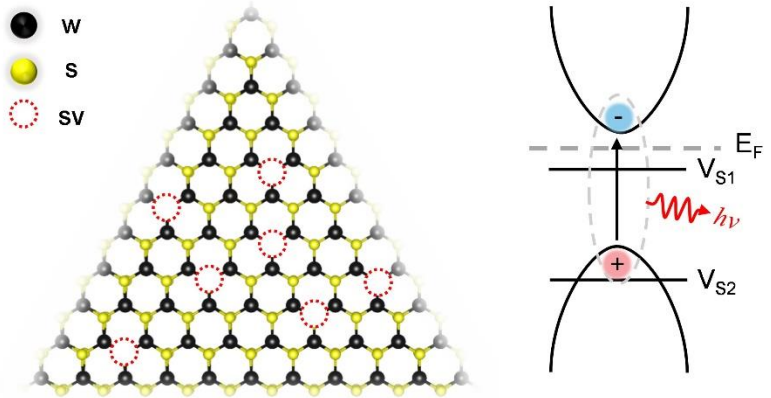

Figure 1. Schematic of sulfur vacancies in monolayer WS_2. Left: Ball-and-stick model of sulfur vacancies in monolayer WS_2, where the black ball, yellow ball, and red dashed circle represent tungsten (W), sulfur (S), and sulfur vacancies (SV), respectively. Right: Illustration of the band structure in the K valley of WS_2 with a sulfur vacancy.

Here, we adopt the salt-assisted 2.0 CVD technique[38-40] for fabricating monolayer WS_2. First, the precursor (sodium tungstate aqueous solution (Na_2WO_4)) was spin-coated onto a 4-inch SiO_2/Si substrate. Subsequently, the substrate with the precursor was added during the CVD process. The details of the synthesis procedure are discussed in the METHODS section and illustrated in Figures S1 and S2. Finally, H_2S gas was added as the sulfurization source to form WS_2. In this process, H_2S, carried by Ar gas, was introduced from the left side to the right side of the CVD, leading to a uniform sulfurization concentration during CVD. H_2S is expected to have a higher uniformity than sulfur vapor. However, uniformity of the sulfurization concentration leads to sulfur vacancy formation during the CVD process. Therefore, we used a controllable H_2S flow rate to regulate the number of sulfur vacancies. The sulfur vacancies at two different H_2S flow rates were investigated using a high-resolution high-angle annular dark-field (HAADF) scanning transmission electron microscopy (STEM), as shown in Figure S3. Sulfur vacancies were identified as the dominant type of defect. The sulfur vacancy densities were 0.14 and 0.07 nm^{-2} for the 5- and 10-sccm H_2S flow rates, respectively. HAADF-STEM images of the sulfur vacancies are shown in Figure 2. Figure S4 presents the PL intensity at the three different flow rates of the H_2S monolayer WS_2 synthesis. The PL intensity of monolayer WS_2 increases with decreasing H_2S flow rate, which is attributed to sulfur vacancies. In general, a stronger PL intensity is associated with more sulfur vacancies. Our results indicate that the number of sulfur vacancies can be engineered by adjusting the H_2S flow rate for sulfurization.

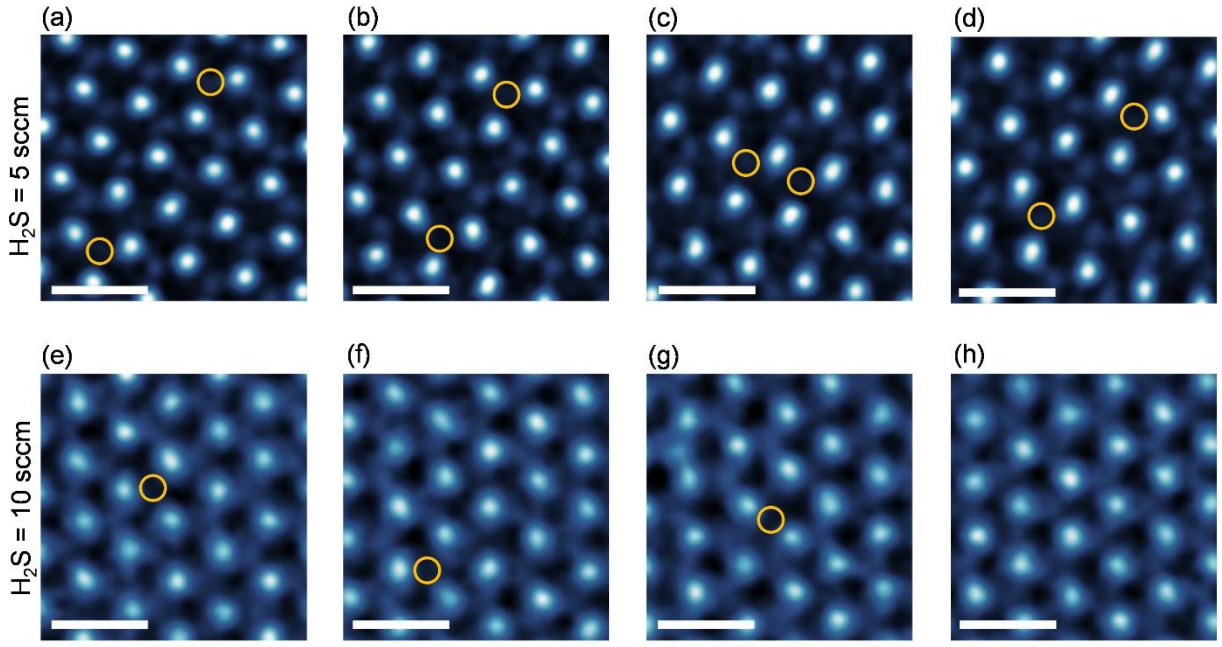

Figure 2. Atomic-resolved HAADF-STEM images to reveal the sulfur vacancies. Sulfur vacancy defects in monolayer WS_2 with different H_2S flow rates during synthesis: (a)–(d) H_2S = 5 sccm; (e)–(h) H_2S = 10 sccm. The scale bars are 0.5 nm.

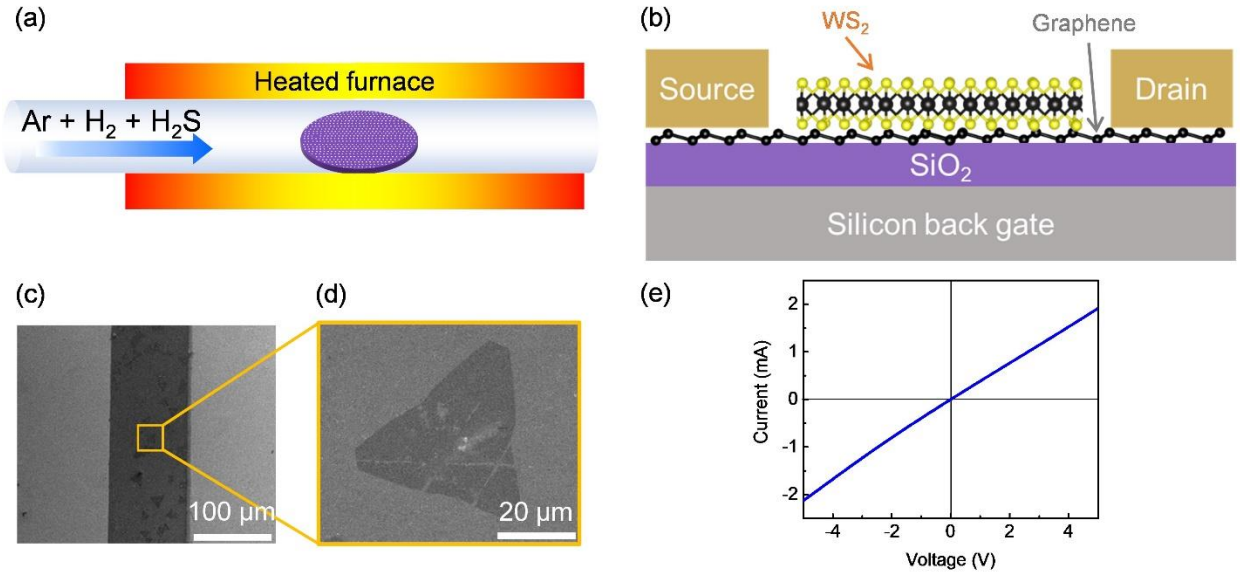

Figure 3. Schematic of the graphene-based heterostructure photodetector. (a) Schematic illustration of using the vapor–liquid–solid method to synthesize monolayer WS_2 using H_2S gas as a sulfurization source. (b) Schematic of the side view of the device configuration composed of vertical stacking of monolayer

WS_2/graphene heterostructures. Scanning electron microscopy images of (c) the heterostructures device and (d) an enlarged image of a monolayer WS_2 flake. The gap between the source and drain was 460 μm. (e) *I*–*V* characterization of graphene-based heterostructure device.

To examine the relationship between the PL intensity and photodetector ability of monolayer WS_2, ~10 WS_2/G heterostructure devices were fabricated. The device configuration of the WS_2/G heterostructure photodetector is shown in Figure 3b. A monolayer graphene film was prepared by CVD and transferred onto a SiO_2/Si substrate, which was used as the conductive layer to transport photoexcited carriers in WS_2. Monolayer WS_2 flakes were then transferred onto a SiO_2/Si substrate with a graphene layer. Figures 3c and 3d show scanning electron microscopy images of the WS_2/G heterostructure photodetector with Au electrodes. Figure 3e shows the current–voltage (*I*–*V*) plot of the WS_2/G photodetector, which exhibits an ohmic contact between the Au electrode and the heterostructure.

The Raman spectra of the transferred graphene, monolayer WS_2, and the WS_2/G heterostructure are shown in Figure 4a. Typical graphene and 2D graphene Raman peaks were observed at 1583 and 2678 cm^{-1}, respectively. The Raman intensity ratio of the graphene and 2D peaks equals 2, indicating single layer characteristic of the graphene. Figure 4b shows the PL spectra of flakes 1 and 2. Flakes 1 and 2 were synthesized using H_2S at 10 and 5 sccm, respectively. Flake 2 exhibits a stronger PL intensity than flake 1 of the A-exciton peak of WS_2. The A-exciton peak position was slightly redshifted to 625 nm in flake 2, whereas the peak position of flake 1 was slightly blueshifted to 620 nm. In general, the redshift of PL in TMD materials can be attributed to compressive strain[41] or higher carrier density.[42] To investigate the strain and doping effects, we used Raman spectroscopy on the flakes (Figures 4c–4e). The three major Raman modes, E^1_{2g}, A_{1g}, and LA (*M*), of flakes 1 and 2 are discussed below. We observed that the strain-related

E^1_{2g} mode exhibited a slight blueshift and redshift in flakes 1 and 2, respectively, compared to exfoliated WS_2,[43] indicating the tensile strain effect, which can be attributed to the surface uniformity of the graphene layer. Similarly, flake 1 redshifts by only ~0.5 cm^{-1} relative to flake 2 of the doping-related A_{1g} mode, implying similar carrier doping in flakes 1 and 2.[44, 45] The LA(M) mode at 176 cm^{-1} is the longitudinal acoustic phonon at the Brillouin zone M point, which implies the presence of defects or disorders that satisfy q = 0 of the Raman selection rule. Additionally, the intensity of LA(M), I(LA), is proportional to L_D^{-2}, where L_D is the average interdefect distance.[46] Therefore, the greater I(LA) value in flake 2, which has a large number of defects, can be attributed to sulfur vacancies. As previously reported,[36, 47] these sulfur-vacancy-related defects trap excitons and prolong the exciton lifetime (τ_e), resulting in enhanced PL intensity (I_{PL}) because $I_{PL} \propto \frac{\tau_e}{\tau_r}$, where τ_r is the radiative recombination time.

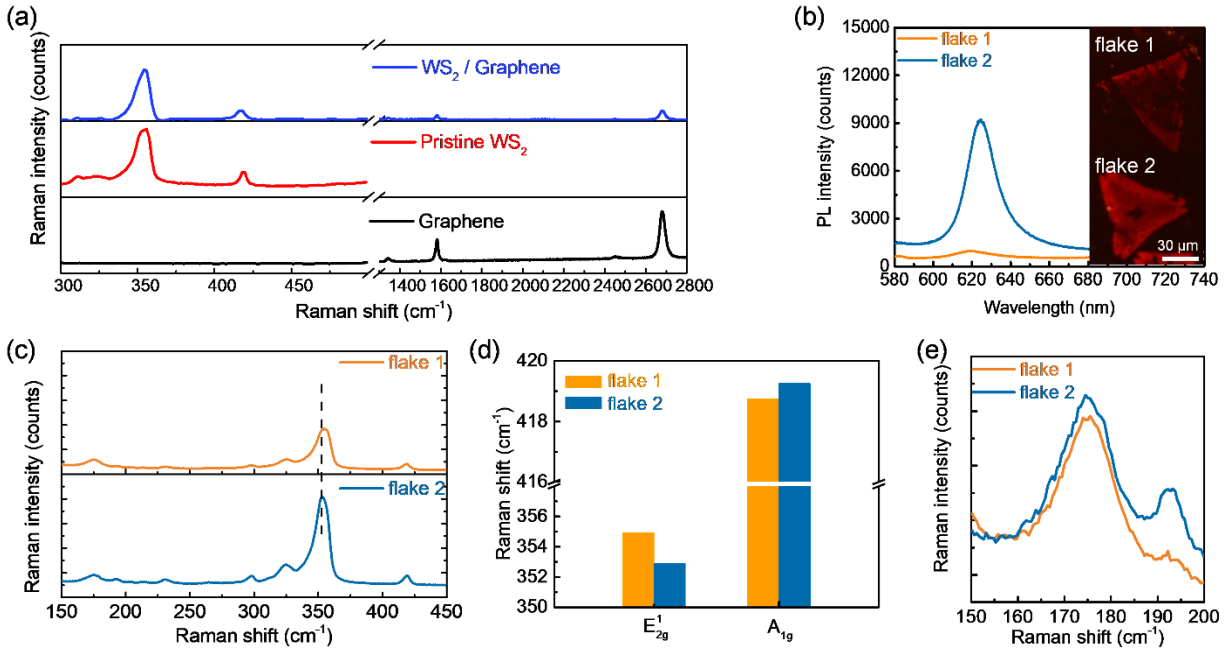

Figure 4. Characterization of WS_2/G heterostructure photodetector device. (a) Raman spectra of the as-transferred graphene, as-grown WS_2 (pristine WS_2), and WS_2 transferred onto the graphene heterostructure device (WS_2/G). (b) PL measurement of flakes 1 and 2. The inset images are the PL images of flakes 1 and 2.

(c)–(e) Raman measurement of flakes 1 and 2. (d) Raman frequency shifts of the E_{2g}^{1} and A_{1g} modes. (e) Raman LA(*M*) mode of flakes 1 and 2.

To understand the defects that influence the optoelectronic properties, WS_2/G heterostructure photodetectors of flakes 1 and 2 (referred to as PD 1 and PD 2, respectively) were characterized. Figure 5a shows the temporal photoresponse of PD 1 and PD 2 with a 532-nm laser switched on and off. Interestingly, PD 1 (flake 1) exhibited a higher photocurrent and a weaker PL intensity; in contrast, PD 2 (flake 2) exhibited a lower photocurrent and a stronger PL intensity. Here, the electrons are photoexcited from the valence band to the conduction band, and a portion of the electrons easily relax and recombine with the holes in the valence band to emit photons. Some electrons were trapped by V_{S1} and gave rise to recombination with holes in V_{S2} or the valance band to emit photons. Other electrons drifted to graphene and generated a photocurrent (see the inset of Figure 5b). Figure 5b summarizes the measured photocurrents and their correlation with the PL intensity for various monolayer WS_2 flakes on the graphene photodetector. WS_2 flakes were prepared with H_2S flow rates ranging from 5 to 15 sccm. We found that monolayer WS_2 flakes on the graphene photodetector exhibit a negative correlation between PL intensity and photocurrent, meaning that regions with high PL intensity have lower photocurrent. This can be attributed to defects. The sulfur vacancy creates defect-bound excitons and increases the radiative recombination rate and the PL intensity. However, the defects also reduce the carrier diffusion length, which increases the probability of carrier recombination before reaching the electrodes and thus lowers the photocurrent.

Furthermore, we evaluated the figure of merit of the WS_2/G photodetectors, such as responsivity (*R*), detectivity (*D*), and dynamic time photoresponse of the photodetectors. The photocurrent as a function of the light intensity was plotted on a logarithmic scale, as shown in

Figure 5c. The photocurrent I_{PC} exhibits a nonlinear dependence on the light intensity and can be fitted using

$$I_{\mathrm{PC}} = AP^{\alpha}, \tag{1}$$

where A and α are fitting constants and P is the light intensity. The fitting parameters α of PD 1 and PD 2 are 0.13 and 0.14, respectively. This nonlinear dependence of the photocurrent on the light intensity observed in the photoconductor implies electron–hole trapping and recombination. Responsivity (R) and detectivity (D), which are used to characterize the figure of merit of a photodetector, are defined as

$$R = \frac{I_{\mathrm{PC}}}{P} \tag{2}$$

and

$$D = R\sqrt{\frac{A}{2eI_{\mathrm{dark}}}}, \tag{3}$$

where A is the area of the photosensitive region of the photodetector. The diameter of the laser beam was ~30 μm. The photoresponsivity and detectivity as a function of the light power were calculated according to Equations (3) and (4), as shown in Figure 5d. The dynamic time response property is important for a photodetector. We measured the time-dependent photoresponse under illumination, and the results are shown in Figure S5. The rise and decay times were 15 and 115 ms, respectively, which are defined as the times required for 10% and 90% signal amplitude changes. Such a temporal photoresponse among 2D-material-based photodetectors results from the photoexcited electrons from WS_2 to graphene and are driven by the high carrier mobility of graphene, which improved the response time compared to that of monolayer TMD photodetectors.

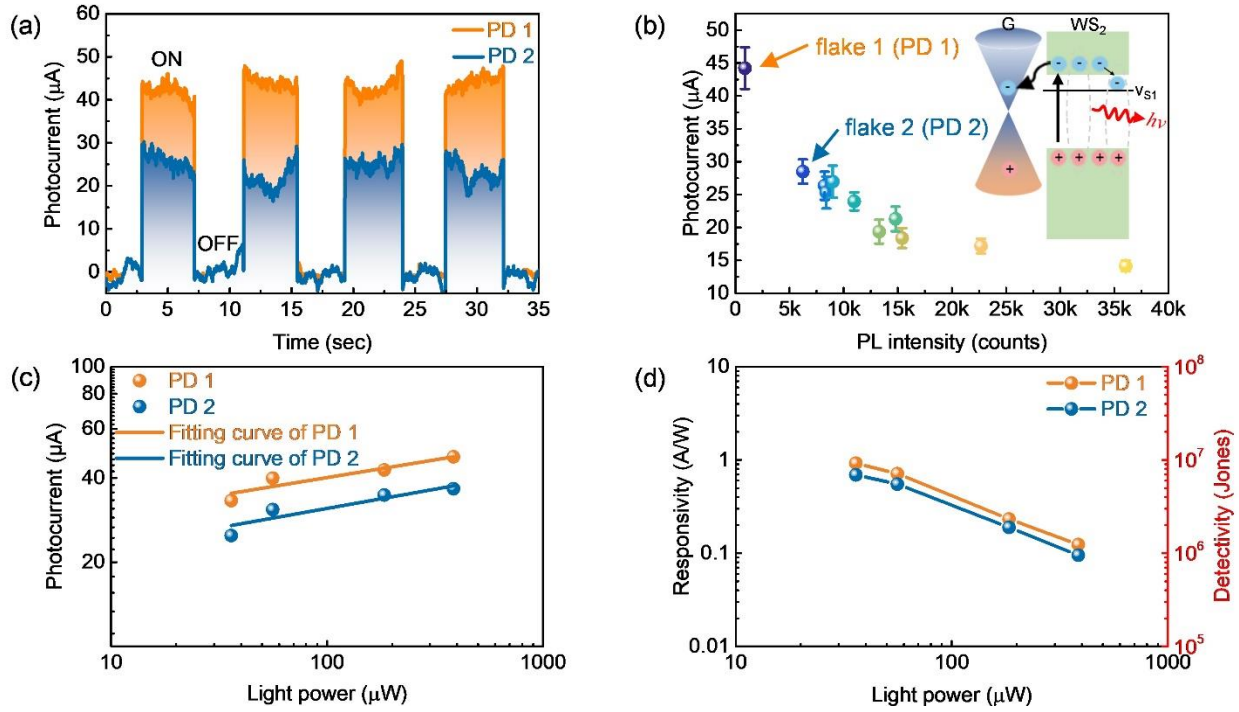

Figure 5. Optoelectronic characterizations of PD 1 and PD 2. (a) Normalized temporary photoresponse of PD 1 and PD 2 (V_{DS} = −5 V; V_{BG} = 0 V). The opposite signs of the photocurrent and V_{DS} suggest that the graphene exhibited p-type characteristics. (b) Photocurrent distributions with respect to the PL intensity of various flakes with a 532-nm continuous-wave (CW) laser as a light source. The irradiance was 46 W/cm^{-2} for (a) and (b). The inset illustrates the relationship between PL and the photocurrent promoted by the defect. (c) Photocurrent as a function of light power. (d) Responsivity and detectivity as a function of light power.

Additionally, photoresponsivity can be enhanced by applying a positive back-gate voltage (V_{BG}). Figure 6 shows the photocurrent and photoresponsivity of PD 1 obtained by applying different drain–source voltages (VDSs) and back-gate voltages (VBGs). High responsivity (5 A/W) can be achieved at V_{BG} = 30 V and V_{DS} = −5 V, where the position of the graphene Fermi level shifts, resulting in no barrier for electron flow from WS_2 to graphene. The temporal photoresponse of light illumination with the application of gate voltage is shown in Figure S5. By applying a positive gate voltage, the barrier-free graphene and WS_2 interface decreased the response time. Moreover, when V_{BG} = −10 V, the photocurrent decreased to zero. This is because the Fermi level

downshift led to the formation of a barrier between WS_2 and graphene; thus, the photoexcited carriers in WS_2 were forbidden from being transferred to graphene. We can further deduce the photogain, which is defined as $G = Rhc/e\lambda$, where h, c, and λ are Plank's constant, the speed of light, and the excitation wavelength, respectively. Photogain G can reach 11.65 electrons per photon at the maximum responsivity. This active tunability is useful in photodetectors because it allows us to control the state (on and off) and adjust the required sensitivity depending on the light power to be detected. In table S1, we summarize the recent works on TMDs based photodetectors. Our works demonstrate good responsivity and detectivity, as well as defect control of the device.

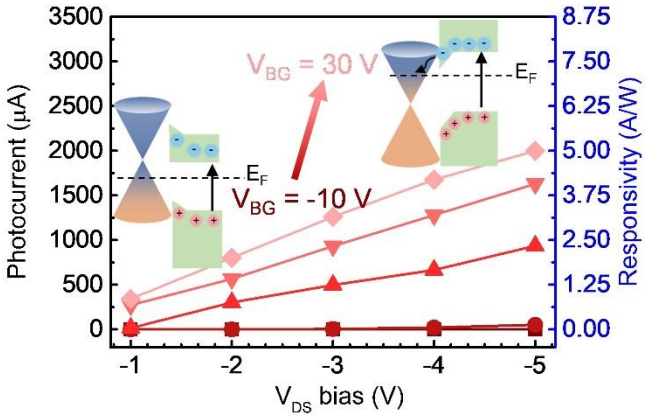

Figure 6. Photocurrent and responsivity as a function of V_{DS} at different back-gate voltage (V_{BG}). The light intensity was 400 μW. Back-gate voltages of −10, 0, 10, 20, and 30 V were applied. The insets illustrate the band diagram of graphene and WS_2 with different V_{BG} values.

4. CONCLUSIONS

In summary, we investigated the relationship between the PL intensity and photocurrent of monolayer WS_2 flakes by controlling the sulfur vacancies of monolayer WS_2 by tuning the H_2S gas flow rate during CVD synthesis. The optoelectronic properties were investigated by constructing WS_2 flakes on graphene photodetectors. We found that the PL intensity and photocurrent were negatively correlated. The sulfur vacancies cause an increase in the PL intensity by introducing defect states to trap the carriers and decrease the number of carriers moving to graphene. Our work has demonstrated that constructing TMD-based photodetectors, including TMD heterostructures, is an efficient and rapid method for choosing highly responsive TMD flakes based on PL intensities. Our findings offer new insights into the development of TMD-based optoelectronic devices. The potential applications of the WS_2/G heterostructure photodetectors could be in high-speed optical communications, ultra-low light imaging, plasmonic near-fields detection[48], flexible electronics and integrated optoelectronic systems.

Appendix A.

Supplementary data Supplementary data to this article can be found online at:XXX

AUTHOR INFORMATION

Corresponding Author

Email: kpchen@nctu.edu.tw

ORCID

Min-Wen Yu: 0000-0003-4173-8813

Chia-Hung Wu: 0000-0003-4489- 3050

Satoshi Ishii: 0000-0003-0731-8428

Jun Kikkawa: 0000-0003-0659-1844

Tien-Chang Lu: 0000-0003-4192-9919

Kuo-Ping Chen: 0000-0001-6256-9145

Author Contributions

M.-W. Y., Y.-T. L., K.-P. C., and S.I. initiated the work. M.-W., Y.-T. L., C.-H. W., T.-J. W., and J.-H. C. contributed the sample fabrication and characterization. J. K. and S. I. work on the STEM measurement. M.-W. Y. drafted the manuscript and revised by T.-C. L., K.-P. C., and S.I. All the authors discussed the results and commented on the manuscript.

Funding Sources

This work is supported by the Higher Education Sprout Project of the National Yang Ming Chiao Tung University, Ministry of Education and the Ministry of Science and Technology (NSTC 110-

2923-E-007 -012 -MY2; 110-2221-E-007 -130 -MY3; 111-2628-E-007-021; 111-2119-M-A49-006) and Kakenhi from JSPS, Japan (22H01917). M.-W. Yu would like to thank Overseas Research Project Subsidies (sponsored by the Ministry of Education, Taiwan and National Yang Ming Chiao Tung University, Taiwan) and International Cooperative Graduate Program (sponsored by National Institute for Materials Science, Japan).

NOTES

The authors declare no competing interests.

ACKNOWLEDGMENT

We acknowledge Dr. Shisheng Li's fruitful discussion on the synthesis of WS_2 with the VLS method.

REFERENCE

1. Lemme, M. C.; Akinwande, D.; Huyghebaert, C.; Stampfer, C., 2D materials for future heterogeneous electronics. *Nat. Commun.* **2022,** *13* (1), 1-5.
2. Liu, Y.; Duan, X.; Shin, H.-J.; Park, S.; Huang, Y.; Duan, X., Promises and prospects of two-dimensional transistors. *Nature* **2021,** *591* (7848), 43-53.
3. Mueller, T.; Xia, F.; Avouris, P., Graphene photodetectors for high-speed optical communications. *Nature photonics* **2010,** *4* (5), 297-301.
4. Yan, K.; Wu, D.; Peng, H.; Jin, L.; Fu, Q.; Bao, X.; Liu, Z., Modulation-doped growth of mosaic graphene with single-crystalline p–n junctions for efficient photocurrent generation. *Nat. Commun.* **2012,** *3* (1), 1-7.
5. Mak, K. F.; Shan, J., Photonics and optoelectronics of 2D semiconductor transition metal dichalcogenides. *Nature Photonics* **2016,** *10* (4), 216-226.
6. Xie, Y.; Zhang, B.; Wang, S.; Wang, D.; Wang, A.; Wang, Z.; Yu, H.; Zhang, H.; Chen, Y.; Zhao, M., Ultrabroadband MoS2 photodetector with spectral response from 445 to 2717 nm. *Advanced Materials* **2017,** *29* (17), 1605972.
7. Kufer, D.; Konstantatos, G., Highly sensitive, encapsulated MoS2 photodetector with gate controllable gain and speed. *Nano Lett.* **2015,** *15* (11), 7307-7313.
8. Fan, Y.; Zhou, Y.; Wang, X.; Tan, H.; Rong, Y.; Warner, J. H., Photoinduced Schottky barrier lowering in 2D monolayer WS2 photodetectors. *Advanced Optical Materials* **2016,** *4* (10), 1573-1581.
9. Tsai, T.-H.; Liang, Z.-Y.; Lin, Y.-C.; Wang, C.-C.; Lin, K.-I.; Suenaga, K.; Chiu, P.-W., Photogating WS2 photodetectors using embedded WSe2 charge puddles. *ACS Nano* **2020,** *14* (4), 4559-4566.
10. Wang, C.; Yang, F.; Gao, Y., The highly-efficient light-emitting diodes based on transition metal dichalcogenides: from architecture to performance. *Nanoscale Advances* **2020,** *2* (10), 4323-4340.
11. Palacios-Berraquero, C.; Palacios-Berraquero, C., Atomically-thin quantum light emitting diodes. *Quantum confined excitons in 2-dimensional materials* **2018**, 71-89.
12. Chang, Y.-H.; Lin, Y.-S.; Singh, K. J.; Lin, H.-T.; Chang, C.-Y.; Chen, Z.-Z.; Zhang, Y.-W.; Lin, S.-Y.; Kuo, H.-C.; Shih, M.-H., AC-driven multicolor electroluminescence from a hybrid WSe 2 monolayer/AlGaInP quantum well light-emitting device. *Nanoscale* **2023**.
13. Lin, H. T.; Chang, C. Y.; Yu, C. L.; Lee, A. B.; Gu, S. Y.; Lu, L. S.; Zhang, Y. W.; Lin, S. Y.; Chang, W. H.; Chang, S. W., Boost Lasing Performances of 2D Semiconductor in a Hybrid Tungsten Diselenide Monolayer/Cadmium Selenide Quantum Dots Microcavity Laser. *Advanced Optical Materials* **2022,** *10* (20), 2200799.
14. James Singh, K.; Ciou, H.-H.; Chang, Y.-H.; Lin, Y.-S.; Lin, H.-T.; Tsai, P.-C.; Lin, S.-Y.; Shih, M.-H.; Kuo, H.-C., Optical Mode Tuning of Monolayer Tungsten Diselenide (WSe2) by Integrating with One-Dimensional Photonic Crystal through Exciton–Photon Coupling. *Nanomaterials* **2022,** *12* (3), 425.
15. Dias, A.; Braganca, H.; de Mendonca, J. P. A.; Da Silva, J. L., Excitonic effects on two-dimensional transition-metal dichalcogenide monolayers: impact on solar cell efficiency. *ACS Applied Energy Materials* **2021,** *4* (4), 3265-3278.
16. Nassiri Nazif, K.; Daus, A.; Hong, J.; Lee, N.; Vaziri, S.; Kumar, A.; Nitta, F.; Chen, M. E.; Kananian, S.; Islam, R., High-specific-power flexible transition metal dichalcogenide solar cells. *Nat. Commun.* **2021,** *12* (1), 7034.

17. Shen, P.-C.; Su, C.; Lin, Y.; Chou, A.-S.; Cheng, C.-C.; Park, J.-H.; Chiu, M.-H.; Lu, A.-Y.; Tang, H.-L.; Tavakoli, M. M., Ultralow contact resistance between semimetal and monolayer semiconductors. *Nature* **2021,** *593* (7858), 211-217.
18. Lan, C.; Li, C.; Wang, S.; He, T.; Zhou, Z.; Wei, D.; Guo, H.; Yang, H.; Liu, Y., Highly responsive and broadband photodetectors based on WS 2–graphene van der Waals epitaxial heterostructures. *Journal of Materials Chemistry C* **2017,** *5* (6), 1494-1500.
19. Zhang, W.; Chuu, C.-P.; Huang, J.-K.; Chen, C.-H.; Tsai, M.-L.; Chang, Y.-H.; Liang, C.-T.; Chen, Y.-Z.; Chueh, Y.-L.; He, J.-H., Ultrahigh-gain photodetectors based on atomically thin graphene-MoS2 heterostructures. *Scientific reports* **2014,** *4* (1), 1-8.
20. Xu, H.; Wu, J.; Feng, Q.; Mao, N.; Wang, C.; Zhang, J., High responsivity and gate tunable graphene-MoS2 hybrid phototransistor. *Small* **2014,** *10* (11), 2300-2306.
21. Lu, D.; Chen, Y.; Kong, L.; Luo, C.; Lu, Z.; Tao, Q.; Song, W.; Ma, L.; Li, Z.; Li, W., Strain-Plasmonic Coupled Broadband Photodetector Based on Monolayer MoS2. *Small* **2022,** *18* (14), 2107104.
22. Thai, K. Y.; Park, I.; Kim, B. J.; Hoang, A. T.; Na, Y.; Park, C. U.; Chae, Y.; Ahn, J.-H., MoS2/graphene photodetector array with strain-modulated photoresponse up to the near-infrared regime. *ACS Nano* **2021,** *15* (8), 12836-12846.
23. Chen, Y.; Deng, W.; Chen, X.; Wu, Y.; Shi, J.; Zheng, J.; Chu, F.; Liu, B.; An, B.; You, C., Carrier mobility tuning of MoS 2 by strain engineering in CVD growth process. *Nano Research* **2021**, 1-7.
24. Sun, J.; Lin, Z.; Jia, X.; Li, H.; Song, C.; Pan, F.; Fang, L.; Zhang, J.; Wang, Y., High-performance 2D WS2 Photodetector Enhanced by Charge-transfer Doping through NH3 Annealing. *Materials Today Physics* **2023**, 101133.
25. Jian, J.; Nan, Y.; Dong, P.; Feng, H.; Zuo, K.; Chang, H., Dependence of the photoelectric performance of the CVD-grown 2D WS2 on the oxygen-doping concentration. *Journal of Alloys and Compounds* **2022,** *895*, 162705.
26. Zhao, H.; Zhang, G.; Yan, B.; Ning, B.; Wang, C.; Zhao, Y.; Shi, X., Substantially enhanced properties of 2D WS2 by high concentration of erbium doping against tungsten vacancy formation. *Research* **2022,** *2022*.
27. Jang, Y.; Yeo, S.; Kim, H.; Kim, S.-H., Wafer-scale, conformal and direct growth of MoS2 thin films by atomic layer deposition. *Applied Surface Science* **2016,** *365*, 160-165.
28. Mattinen, M.; Hatanpää, T.; Sarnet, T.; Mizohata, K.; Meinander, K.; King, P. J.; Khriachtchev, L.; Räisänen, J.; Ritala, M.; Leskelä, M., Atomic layer deposition of crystalline MoS2 thin films: new molybdenum precursor for low-temperature film growth. *Advanced Materials Interfaces* **2017,** *4* (18), 1700123.
29. Eichfeld, S. M.; Hossain, L.; Lin, Y.-C.; Piasecki, A. F.; Kupp, B.; Birdwell, A. G.; Burke, R. A.; Lu, N.; Peng, X.; Li, J., Highly scalable, atomically thin WSe2 grown via metal–organic chemical vapor deposition. *ACS Nano* **2015,** *9* (2), 2080-2087.
30. Kang, K.; Xie, S.; Huang, L.; Han, Y.; Huang, P. Y.; Mak, K. F.; Kim, C.-J.; Muller, D.; Park, J., High-mobility three-atom-thick semiconducting films with wafer-scale homogeneity. *Nature* **2015,** *520* (7549), 656-660.
31. Lee, Y. H.; Zhang, X. Q.; Zhang, W.; Chang, M. T.; Lin, C. T.; Chang, K. D.; Yu, Y. C.; Wang, J. T. W.; Chang, C. S.; Li, L. J., Synthesis of large-area MoS2 atomic layers with chemical vapor deposition. *Advanced materials* **2012,** *24* (17), 2320-2325.
32. Wang, X.; Gong, Y.; Shi, G.; Chow, W. L.; Keyshar, K.; Ye, G.; Vajtai, R.; Lou, J.; Liu, Z.; Ringe, E., Chemical vapor deposition growth of crystalline monolayer MoSe2. *ACS*

Nano **2014,** *8* (5), 5125-5131.
33. Van Der Zande, A. M.; Huang, P. Y.; Chenet, D. A.; Berkelbach, T. C.; You, Y.; Lee, G.-H.; Heinz, T. F.; Reichman, D. R.; Muller, D. A.; Hone, J. C., Grains and grain boundaries in highly crystalline monolayer molybdenum disulphide. *Nat. Mater.* **2013,** *12* (6), 554-561.
34. Yang, X.; Li, S.; Ikeda, N.; Sakuma, Y., Oxide scale sublimation chemical vapor deposition for controllable growth of monolayer MoS2 crystals. *Small Methods* **2022,** *6* (2), 2101107.
35. Addou, R.; Colombo, L.; Wallace, R. M., Surface defects on natural MoS2. *ACS Appl. Mater. Interfaces* **2015,** *7* (22), 11921-11929.
36. Bretscher, H.; Li, Z.; Xiao, J.; Qiu, D. Y.; Refaely-Abramson, S.; Alexander-Webber, J. A.; Tanoh, A.; Fan, Y.; Delport, G.; Williams, C. A., Rational passivation of sulfur vacancy defects in two-dimensional transition metal dichalcogenides. *ACS Nano* **2021,** *15* (5), 8780-8789.
37. Refaely-Abramson, S.; Qiu, D. Y.; Louie, S. G.; Neaton, J. B., Defect-induced modification of low-lying excitons and valley selectivity in monolayer transition metal dichalcogenides. *Phys. Rev. Lett.* **2018,** *121* (16), 167402.
38. Li, S., Salt-assisted chemical vapor deposition of two-dimensional transition metal dichalcogenides. *Iscience* **2021,** *24* (11), 103229.
39. Li, S.; Lin, Y.-C.; Liu, X.-Y.; Hu, Z.; Wu, J.; Nakajima, H.; Liu, S.; Okazaki, T.; Chen, W.; Minari, T., Wafer-scale and deterministic patterned growth of monolayer MoS 2 via vapor–liquid–solid method. *Nanoscale* **2019,** *11* (34), 16122-16129.
40. Liu, H.; Qi, G.; Tang, C.; Chen, M.; Chen, Y.; Shu, Z.; Xiang, H.; Jin, Y.; Wang, S.; Li, H., Growth of large-area homogeneous monolayer transition-metal disulfides via a molten liquid intermediate process. *ACS Appl. Mater. Interfaces* **2020,** *12* (11), 13174-13181.
41. Wang, Y.; Cong, C.; Yang, W.; Shang, J.; Peimyoo, N.; Chen, Y.; Kang, J.; Wang, J.; Huang, W.; Yu, T., Strain-induced direct–indirect bandgap transition and phonon modulation in monolayer WS2. *Nano Research* **2015,** *8* (8), 2562-2572.
42. Lee, H. S.; Kim, M. S.; Kim, H.; Lee, Y. H., Identifying multiexcitons in mo s 2 monolayers at room temperature. *Phys. Rev. B* **2016,** *93* (14), 140409.
43. Berkdemir, A.; Gutiérrez, H. R.; Botello-Méndez, A. R.; Perea-López, N.; Elías, A. L.; Chia, C.-I.; Wang, B.; Crespi, V. H.; López-Urías, F.; Charlier, J.-C., Identification of individual and few layers of WS2 using Raman Spectroscopy. *Scientific reports* **2013,** *3* (1), 1-8.
44. Lin, W.-H.; Tseng, W.-S.; Went, C. M.; Teague, M. L.; Rossman, G. R.; Atwater, H. A.; Yeh, N.-C., Nearly 90% circularly polarized emission in monolayer WS2 single crystals by chemical vapor deposition. *ACS Nano* **2019,** *14* (2), 1350-1359.
45. Jeong, H. Y.; Jin, Y.; Yun, S. J.; Zhao, J.; Baik, J.; Keum, D. H.; Lee, H. S.; Lee, Y. H., Heterogeneous defect domains in single-crystalline hexagonal WS2. *Advanced Materials* **2017,** *29* (15), 1605043.
46. McCreary, A.; Berkdemir, A.; Wang, J.; Nguyen, M. A.; Elías, A. L.; Perea-López, N.; Fujisawa, K.; Kabius, B.; Carozo, V.; Cullen, D. A., Distinct photoluminescence and Raman spectroscopy signatures for identifying highly crystalline WS2 monolayers produced by different growth methods. *Journal of Materials Research* **2016,** *31* (7), 931-944.
47. McCreary, K. M.; Hanbicki, A. T.; Sivaram, S. V.; Jonker, B. T., A-and B-exciton photoluminescence intensity ratio as a measure of sample quality for transition metal dichalcogenide monolayers. *Apl Materials* **2018,** *6* (11), 111106.
48. Wu, C.-H.; Ku, C.-J.; Yu, M.-W.; Yang, J.-H.; Lu, T.-C.; Lin, T.-R.; Yang, C.-S.; Chen, K.-P., Nonscattering Photodetection in the Propagation of Unidirectional Surface Plasmon

Polaritons Embedded with Graphene. *ACS Appl. Mater. Interfaces* **2022**.